The Free Internet Journal
for Organic Chemistry

Paper

Archive for
Organic Chemistry

Arkivoc **2020**, part v, 59-84

Synthesis and application of a fluorescent "turn-off" triazolyl-coumarin-based fluorescent chemosensor for the sensing of Fe^{3+} ions in aqueous solutions

Neliswa Mama* and Aidan Battison

Department of Chemistry, Nelson Mandela University, P.O Box 77000, Port Elizabeth, 6031, South Africa
Email: neliswa.mama@mandela.ac.za

Received 06-30-2020 **Accepted** 09-16-2020 **Published online** 09-19-2020

Abstract

Two coumarin derivatives containing triazole moieties have been synthesized using "click chemistry" protocol and investigated as chemosensors for the detection of metal ions. These compounds displayed a strong preference for Fe^{3+} ions with complexation resulting in fluorescent quenching. The detection limit of the preferred chemosensor was determined to be 1.4 µM. The preferred triazole-coumarin compound showed greater selectivity towards Fe^{3+} in the presence of competing metal cations. Binding stoichiometry between this triazole-coumarin and Fe^{3+} was shown to occur in a 1:1 ratio between the chemosensor and metal cation. The binding site of Fe^{3+} to the triazole-coumarin was determined using ^{1}H NMR, ^{13}C NMR and molecular modeling studies.

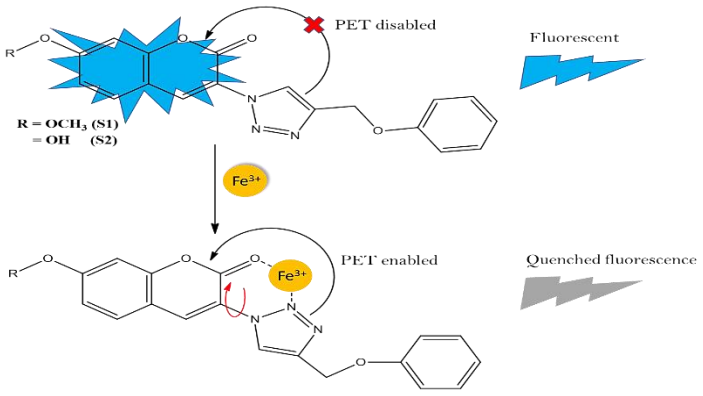

Keywords: Coumarin, triazole, click chemistry, fluorescence, chemosensor, static quenching, molecular modeling

Introduction

The development of fluorescent chemosensors possessing high sensitivity and selectivity for environmentally- and biologically important heavy- and transition metal cations has evolved into a growing field of research due to the significant advantages they offer.[1] Conventional sensing methods such as inductively coupled plasma atomic emission spectrometry (ICP-AES), inductively coupled plasma mass spectrometry (ICP-MS), atomic absorption spectroscopy (AAS) and electrochemical methods are costly and require professional operators.[2] Compared to sophisticated instrumentation, fluorescent chemosensors for analyte detection and analysis have shown to be promising alternatives due to the simple equipment required, cost-effective synthetic procedures and analysis, rapid response times, low detection limits, high resolution and good selectivity and sensitivity.[3,4]

In many fields of application, the analysis of Fe^{3+} ions is of great importance. The majority of these applications including biomedical, environmental, and aquatic systems.[5] Iron is one of the most abundant and indispensable elements in the human body.[6] It is present in hemoglobin and has a crucial effect in oxygen uptake, oxygen metabolism, and electron transfer throughout the body.[7] Furthermore, it serves as a cofactor in many enzymatic reactions and catalysis, neurotransmission, and nucleic acid synthesis, with both deficiency and excess amounts of Fe^{3+} causing various diseases.[8] High concentrations in the body lead to an imbalance between oxidation and antioxidation which can damage proteins and lipids, and can cause nucleic acid mutations.[9–11] In addition, excessive iron concentrations may increase the risks of hemochromatosis, diabetes, osteoporosis, heart and pancreatic disease, *inter alia*.[12] Deficiency in iron can cause anemia and related health concerns such as impaired cognitive function, lethargy, low immunity, liver damage, and cancer.[13,14] Both the excess and deficiency of iron may play a role in neurodegenerative disorders such as Alzheimer's and Parkinson's diseases.[15–18] Estimates of the minimum dietary intake for iron depend on age, gender, activity, physiological status, and iron bioavailability.[19,20]

Iron concentration in surface waters is usually reported to be less than 1 mg/L, but higher concentrations (<50 mg/L) have been reported in groundwater sources. An excess of iron in the environment can also arise from the corrosion of ferrous materials. This leaching of iron into environmental water systems can move through the food chain. It also has a severe impact on the quality of agricultural crops.[21] The maximum acceptable level of iron in water has been set at 0.3 mg/L (nearly 6 μM) by the World Health Organization (WHO).[22,23] It is no surprise that a great deal of time and effort have been devoted towards developing a convenient and efficient method to selectively monitor and detect iron content for pathological studies and environmental protection.

A typical chemosensor consists of two distinct components: a receptor and signaling unit (fluorophore), which can be connected either by chemical bonds or by spacer units. The fluorophore unit is the site of excitation and emission, whilst the receptor subunit is responsible for recognizing and binding to an analyte of interest with high selectivity and efficiency *via* a reversible/non-reversible covalent or non-covalent interaction.[24,25] Recently, coumarins have been used in fluorescent chemosensors due to their high optical activities, high light stabilities, high quantum yields, wide Stokes shifts, ease of tuneability, and low toxicity properties.[26,27] Furthermore, the carbonyl functionality of coumarin can partake in coordination with metal ions, if necessary. This is advantageous for the design of chemosensors as the response will be fast and efficient when analytes are bound to the host probes.[6] Both nitrogen and oxygen atoms are frequently identified as donor atoms which readily combine with transition metal cations, including Fe^{3+}.[28]

Several triazolyl-coumarin-based chemosensors have been developed for metal-ion detection. The favourable fluorescent properties of coumarin derivatives, coupled with the metal-ion-binding abilities of the triazole unit[29], lead to chemosensors that can be used for the recognition and sensing of various metal ions based on changes in the fluorescent properties of the coumarin fluorophore. Previously, we have used the triazole ring as the binding unit in a coumarin-based chemosensor that was found to be a selective ion binder of Cu^{2+}.[30] With this in mind, two triazolyl-coumarin-based chemosensors, (**S1**) and (**S2**) (Figure 1), were synthesized using "click chemistry" protocol. These coumarin derivatives incorporated different substituents (hydroxyl and methoxy groups) at position 7 to improve their fluorescence and solubility in aqueous and organic solvents. The resulting chemosensors were selective for Fe^{3+} in CH_3CN / H_2O solvent mixtures, with changes in their fluorescent properties upon the addition of metal ion solutions.

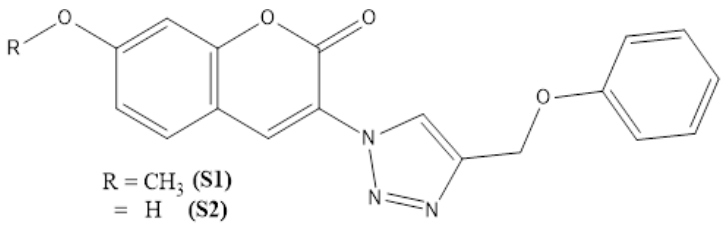

Figure 1. Structures of triazole-coumarin chemosensors (**S1**) and (**S2**).

Results and Discussion

Synthesis of triazolyl coumarin derivatives (S1) and (S2)

The synthesis of triazolyl coumarin derivatives was performed according to the reaction outlined in Scheme 1. Firstly, coumarin derivatives with azide functionalities were prepared according to literature procedures.[31] The final step was achieved using Cu(I) catalyzed 1,3-dipolar cycloaddition in a "click" reaction between coumarin-azide derivatives (**1**) with alkyne derivative (**2**) in THF to afford triazolyl coumarin derivatives (**S1**) and (**S2**) in 80% and 65% yields, respectively. The chemical structures of **S1** and **S2** were confirmed by NMR spectroscopic data. Further confirmation studies were carried out using crystal X-ray diffraction analysis as shown in Figure 2. The single crystal structures of both **S1** and **S2** show the presence of the coumarin ring system with the triazole functionality at position -C3-. The nitrogen atoms of the triazole ring are orientated away from the coumarin carbonyl in both **S1** and **S2** whilst the carbon-carbon double bond of the triazole ring is situated closest to the coumarin-carbonyl functionality.

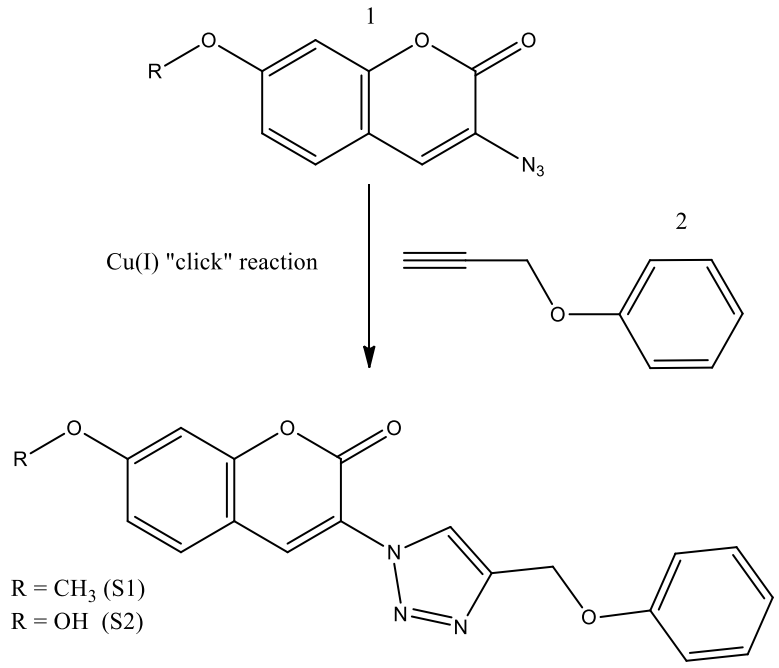

Scheme 1. Synthetic route of triazolyl coumarin derivatives **S1** and **S2**. "Click" reaction conditions: THF, $CuSO_4.5H_2O$, NaAsc and PMDETA.

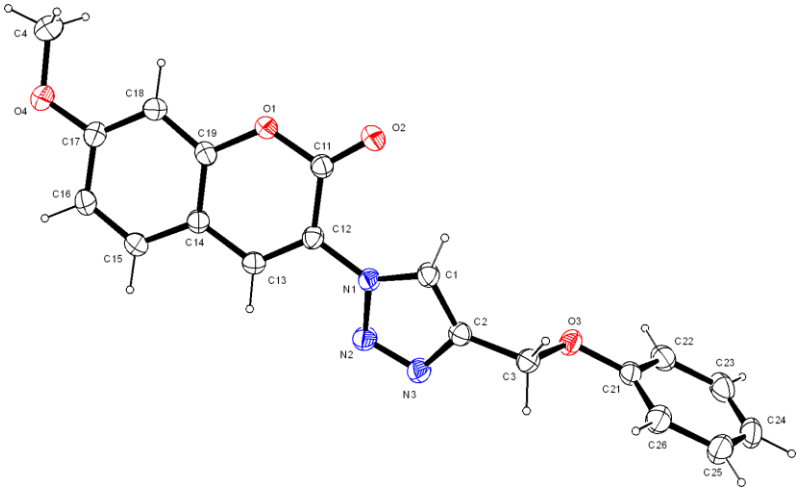

a)

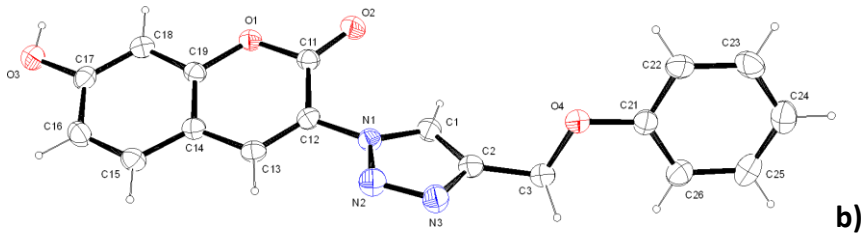

b)

Figure 2. X-ray crystal structures of triazolyl-coumarin derivatives **S1** (a) and **S2** (b).

Studies of the absorption and emission properties of triazolyl-coumarin derivatives (S1) and (S2)

The absorption and emission behaviors of **S1** and **S2** were investigated in acetonitrile and water, respectively. The excitation wavelength for both chemosensors was determined by UV-Vis analysis in acetonitrile. The sensors displayed the same excitation wavelength of 340 nm with the absorption intensity of **S1** being exceptionally greater than that of **S2** (Figure 3a). The emission properties of both chemosensors were further investigated in aqueous media at the same excitation wavelength of 340 nm (Figure 3b). Again, **S1** displayed stronger emission at 420 nm than that of **S2** at a longer wavelength of 480 nm. It is well documented that electron donating groups at position -7- (such as methoxyl and hydroxyl) and electron withdrawing groups at position -3- (such as triazole) induce a push-pull effect which concentrates electron density into the conjugated π-system of the coumarin moiety, thereby enhancing the emissive output (Figure 3c). This is a commonly used method to improve the fluorescence efficiency and intensity of coumarin compounds.[32–35] This difference between the emissive intensities of **S1** and **S2** may be rationalized when the theoretical calculated electron density around the methoxyl and hydroxyl functionalities, coumarin carbonyl, and corresponding triazole moiety is considered. Figure 4 shows the calculated electron density around the -C7- functionalities and the corresponding electron density within the coumarin π-conjugated system and surrounding the triazole ring. It is evident from the larger area of electron deficiency surrounding the three methoxy hydrogen atoms, and greater area of increased electron density surrounding the coumarin carbonyl and triazole moiety of **S1**, that electron density has been pushed/pulled through the conjugated system via the push-pull electronic effect. In this way, emission intensity of **S1** is notably greater than that of **S2**.

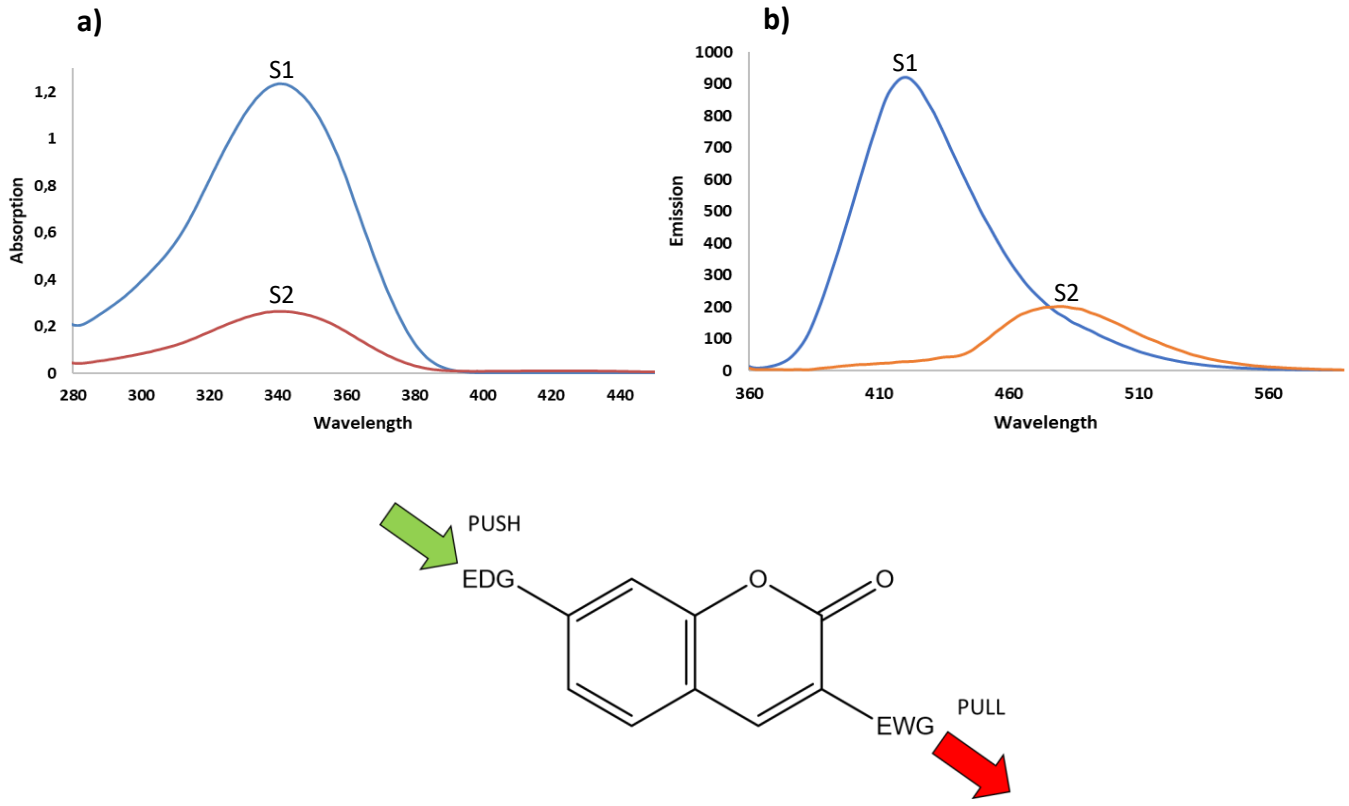

Figure 3. Comparison of the absorption (a) and emission (b) of equal concentration aliquots of **S1** and **S2** in acetonitrile and water, respectively. Excitation conducted at 340 nm; (**c**) Push-pull effect of substituted coumarin molecules.

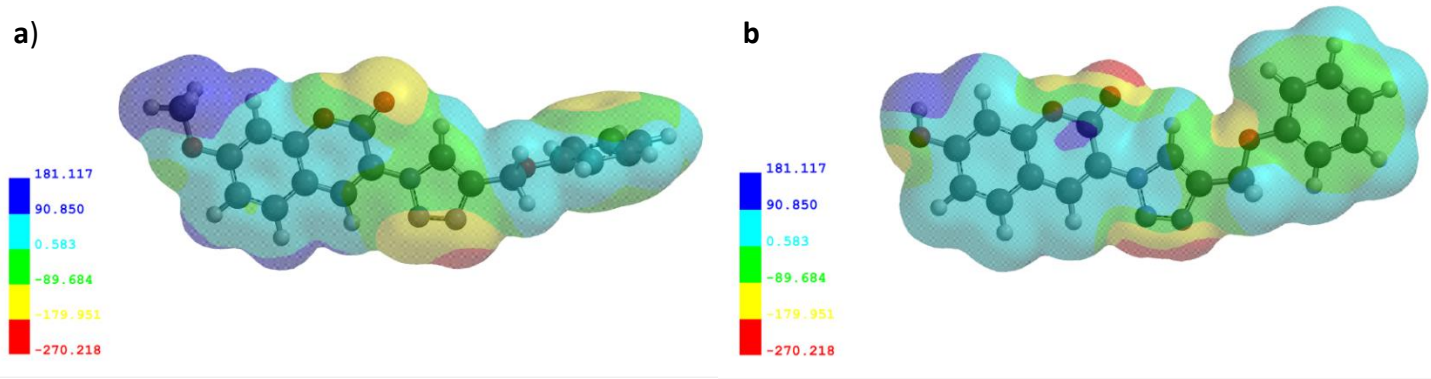

Figure 4. Calculated electronic densities of (a) **S1** and (b) **S2** at MMFF level using Spartan '10 V1.10.

The sensing responses of chemosensors (S1) and (S2) towards various metal ions

The application of **S1** and **S2** as chemosensors for metal cations was studied using fluorescence spectral analysis at room temperature. A range of 16 metal ions were investigated as their nitrate salts in aqueous solution. The experiments were conducted by adding 20 µl aliquots of the selected metal ions (Fe^{2+}, Fe^{3+}, Cd^{2+}, Pb^{2+}, Ag^{+}, Na^{+}, K^{+}, Ca^{2+}, Cr^{3+}, Al^{3+}, Ba^{2+}, Cu^{2+}, Co^{2+}, Hg^{2+}, $Zn^{2+}$and Ni^{2+}) to solutions of compounds **S1** and **S2** in water. Water was chosen as the sensing medium as aqueous sensing is environmentally friendly and greatly preferred. Table 1 shows the emission changes of **S1** and **S2** upon addition of various metals. Metal screening studies were conducted in triplicate.

Table 1. Fluorescent responses of the chemosensors **S1** and **S2** in the presence of selected metal cations in water. Excitation conducted at 340 nm

Metal Cation (20 µL of 0.01 M solutions)	**S1**	**S2**
Fe^{3+}	Strong quenching	Strong quenching
Hg^{2+}, Fe^{2+}, Cd^{2+}, Pb^{2+}, Ag^{+}, Na^{+}, K^{+}, Ca^{2+}, Cr^{3+}, Al^{3+}, Cd^{2+}, Ba^{2+}, Co^{2+}, $Zn^{2+}$and Ni^{2+}	Minimal quenching	Minimal to good quenching

The quenching responses of **S1** and **S2** were observed to be greater for Fe^{3+} than that of the other metal cations indicating a stronger interaction between the chemosensor and Fe^{3+}. Notably, the effect of Fe^{3+} towards quenching was more prominent in **S1** as the emission range where all other metal cations displayed quenching responses was a great deal smaller than that observed in **S2** (Figure 5). Competition studies between Fe^{3+} and other competing metal cations was conducted in water (Figure 6). Notably, **S1** displayed excellent selectivity towards Fe^{3+} in the presence of other competing metal cations. Furthermore, when all competing metal cations were added to solution at once, **S1** still displayed excellent selectivity towards Fe^{3+}. This same selectivity trend towards Fe^{3+} was not observed For **S2** with all other competing metals (Figure 7). For this reason, and the enhanced absorption and emission properties of **S1**, it was chosen for further investigations as a potential chemosensor for quantitative and qualitative sensing of Fe^{3+} ions in aqueous media. The observed quenching response upon Fe^{3+} addition, to the best of our knowledge, can be ascribed to the photo-induced electron transfer (PET) from the chemosensor to the d-orbitals of Fe^{3+}. The electron

deficiency of half-filled d-orbitals increases the electrostatic attraction of the binding site to form stable coordination with Fe^{3+} ions, leading to more quenching of the fluorescence and better selectivity.

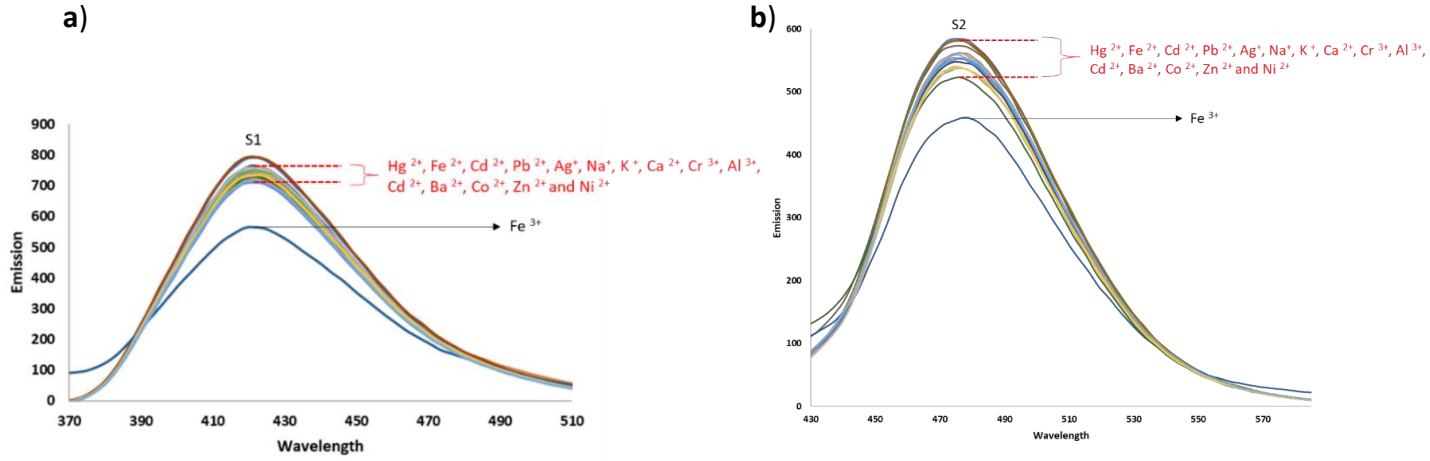

Figure 5. Fluorescent responses of (a) **S1** and (b) **S2** with selected metal cations in water. Excitation: 340 nm.

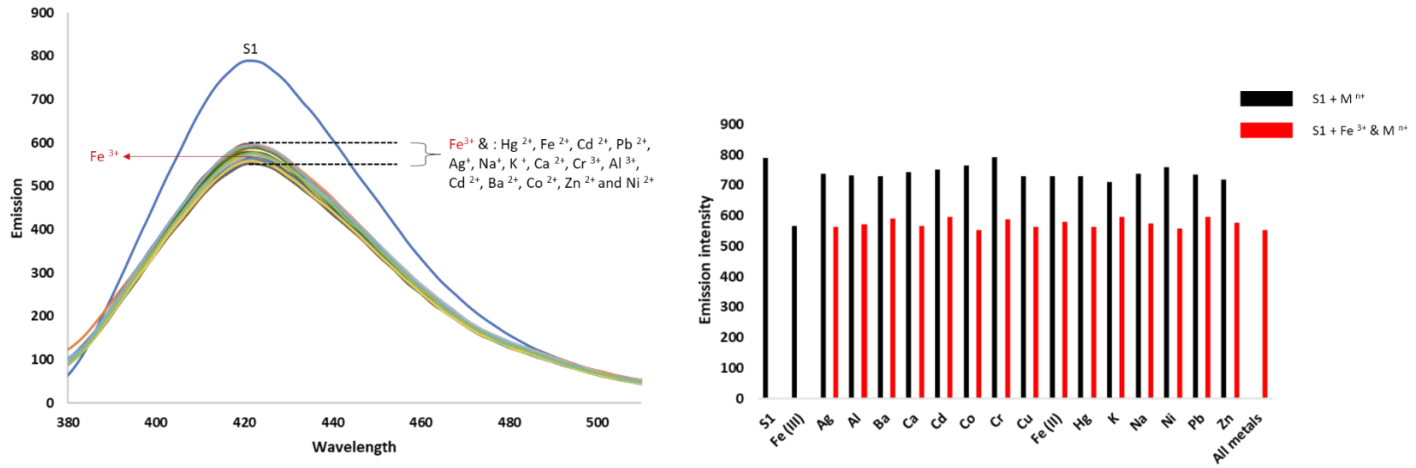

Figure 6. Selectivity of **S1** towards Fe^{3+} with competing metal cations in water. Competition studies were performed in triplicate. Excitation: 340nm.

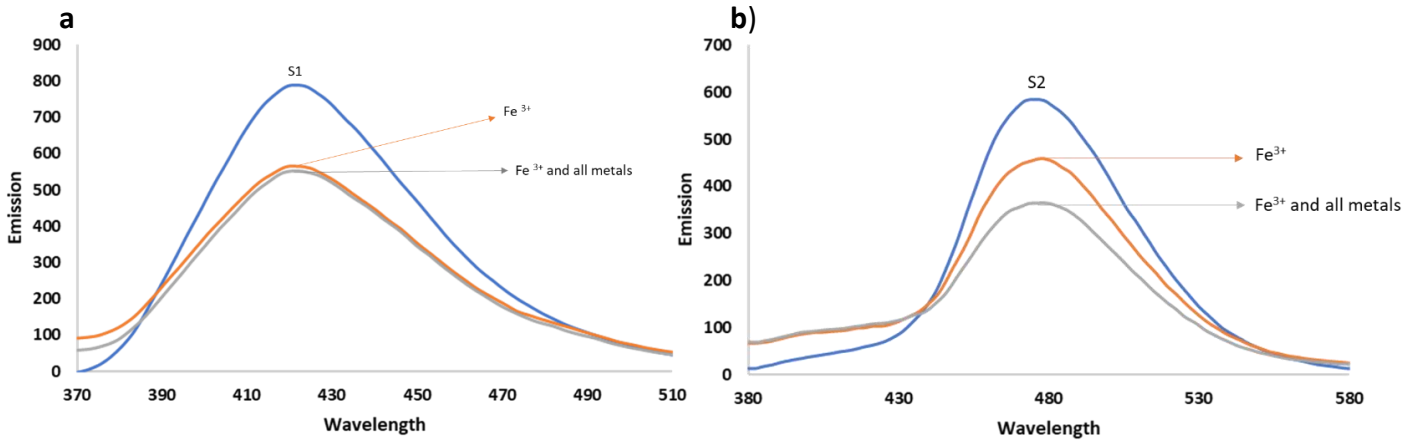

Figure 7. a) Competition of **S1** with Fe^{3+} and all other competing metal cations; b) Competition of **S2** with Fe^{3+} and all other competing cations. Excitation: 340 nm.

Titration studies of S1 in the presence of Fe^{3+}

To gain greater insight into the fluorescent properties of **S1** in the presence of Fe^{3+}, the fluorescence response was investigated with Fe^{3+} in both water and acetonitrile. From this investigation, it is evident how the solvent system used can affect the outcome of the both the emission response and various other properties such as detection limit and binding/association constants *inter alia*. Figure 8 illustrates the variations in the fluorescent intensities of **S1** upon continuous addition of Fe^{3+} aliquots in water and acetonitrile. The titration experiment of **S1** with Fe^{3+} in acetonitrile yielded three new shoulder peaks at longer wavelengths of 445, 487 and 531 nm. The titration of **S1** with Fe^{3+} in water evolved one small new shoulder peak at 487nm at higher concentrations of Fe^{3+}. The Stokes shifts of S1 with Fe^{3+} in water and acetonitrile to longer wavelengths were calculated to be 1 and 8 nm, respectively. To ensure that the quenching response of **S1** towards Fe^{3+} is dependent on analyte addition and that progressive self-quenching from single addition of the analyte does not occur, time-delay studies of **S1** with one aliquot of Fe^{3+} was conducted. Results show that between the initial quenching response of **S1** with a single 20 µL aliquot of the analyte, and after the 20th scan, no additional fluorescent quenching was observed. The quenching response is therefore dependent on analyte addition which is vital for titration analysis (Figure S8, Supplementary Material).

When the polarity of the solvents is taken into consideration, the observations of the new shoulder peaks upon Fe^{3+} titration may be explained. It is known that the fluorescent emission spectra of many fluorophores are sensitive to the polarity of their surrounding environment. Water is more polar than acetonitrile and will therefore have a different effect with cation binding and stability. This may be attributed to the difference in the dipole moments in the ground state and the excited state. If electrically neutral molecules have a larger dipole moment in the excited state than in the ground state, the excited state becomes more stabilized with increasing solvent polarity.[36] The excited states of the compounds are mainly affected by the polarity, refractive index as well as dielectric constants of solvents and also, by the solvation effect of solvents towards compounds.[37] The differences observed between acetonitrile and water could be attributed to factors such as hydrogen bonding. Possible intermolecular hydrogen bonding interactions between water molecules and coumarin carbonyl inhibit the formation of intramolecular hydrogen bonds which can alter the dipole moments of the ground and excited states. This plausible larger dipole moment in the excited state is stabilized in water. Compared to water, acetonitrile is less polar and may not have as great an ability to stabilize this excited state complex. Possible intramolecular hydrogen bonding may result in the

formation of new excited state complexes or vibrational energy levels with increasing Fe^{3+} amounts, resulting in the formation of the three new shoulder peaks at longer wavelengths. The appearance of these new shoulder peaks in acetonitrile gives further justification towards the use of water as the medium of choice for further studies.

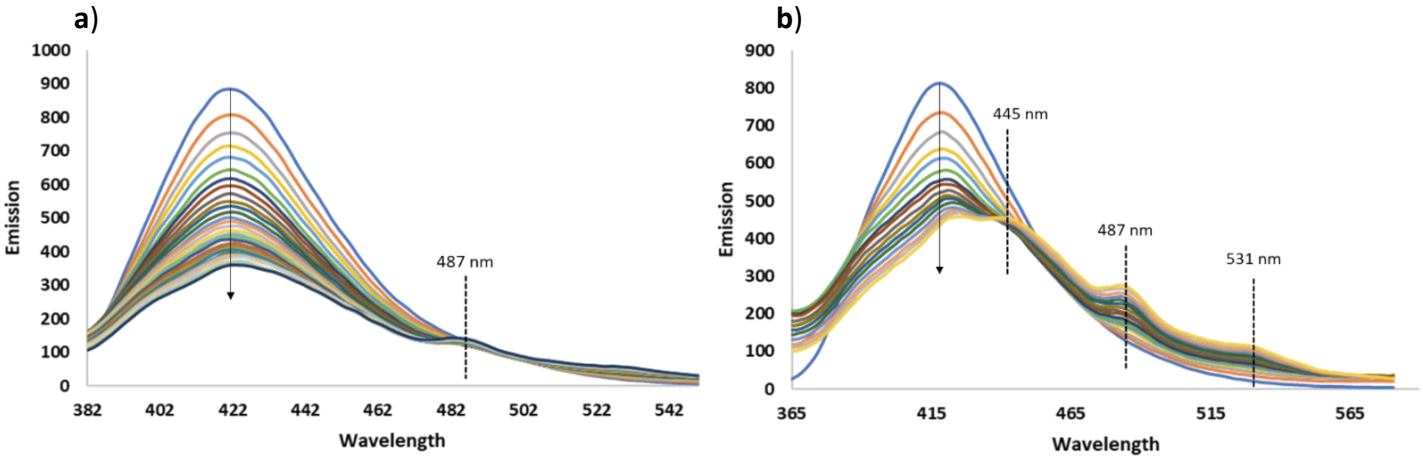

Figure 8. Changes in the fluorescence spectrum of **S1** in a) water and b) acetonitrile upon addition of Fe^{3+} ions. Excitation: 340nm. Titration conducted in triplicate.

Closer consideration of the titration of **S1** in water shows a clear iso-emissive point at 387 nm between the titration amounts of 4 µM to 19 µM additions of Fe^{3+}. At higher concentrations of Fe^{3+} the titration no longer displays this phenomenon (Figure 9a & b).

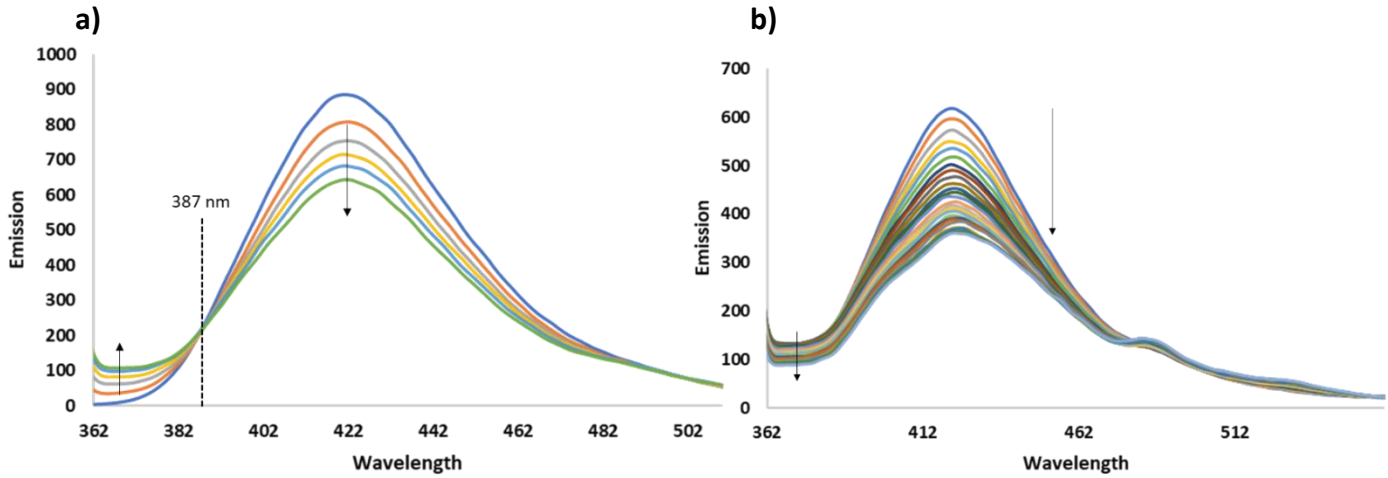

Figure 9. a) Titration of **S1** with 4 to 19 µM additions of Fe^{3+}. A clear iso-emissive point is observed at 387 nm; b) Titration of **S1** with 23 to 106 µM Fe^{3+}, the iso-emissive point is no longer visible.

The formation of iso-emissive points in fluorescent spectrum may be attributed to a number of reasons including ground state binding between **S1** and Fe^{3+} in solution[38], the presence of two absorbing and emitting

species in the system[39], two or more emitting species in the excited state[40], and neutral and ionic forms of the complexes existing in equilibrium in the photo-excited state[41]. Whilst ground state binding between **S1** & Fe^{3+} and more than one emitting species could be a plausible explanations, studies conducted by dos Santos and co-workers describe how complexation induced twisting reduces the effect of the PET quenching from the fluorophore by 'blocking' the pathway of the electron transfer, thus leading to the appearance of the iso-emissive point.[42] Interestingly, a similar conformational change was observed between the X-ray crystallographic structures of **S1** alone and **S1** with Fe^{3+} (Figure 10a & b). Although the complex of **S1** with Fe^{3+} did not crystallize, it did however change the crystal system from triclinic to monoclinic and induced this same twisting of the molecule as described by dos Santos et al. This initial twisting of the molecule at lower concentrations of Fe^{3+} coupled with complexation of S1 and Fe^{3+} in the ground state, and two emitting species at lower concentrations, could explain the appearance of the iso-emissive point. This plausible "twisting" was further verified by computational analysis whereby the triazole ring twists upon metal complexation so the ring nitrogens are located *syn* to the coumarin carbonyl.

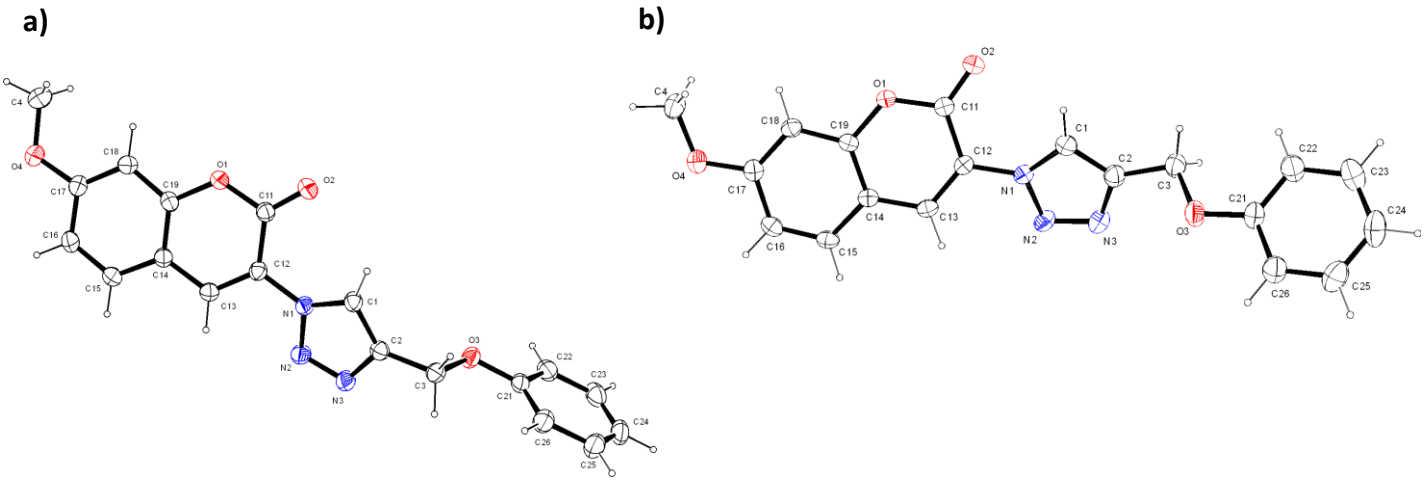

Figure 10. a) Crystal X-Ray diffraction of **S1** before complexation; b) after interaction with Fe^{3+} at lower concentrations.

UV-Vis titration of S1 with Fe^{3+}

The UV-Vis titration of **S1** with Fe^{3+} was conducted in acetonitrile. Fluorescent studies indicated that the same quenching response was visible in acetonitrile and water. High concentrations of **S1** was required for analysis which resulted in precipitation in water thereby altering absorption results, thus acetonitrile was used as the solvent. Figure 11 shows the titration of **S1** with Fe^{3+} in acetonitrile. Evidently, titration lead to increased absorption between 50 and 750 µM Fe^{3+} additions. No visible hypsochromic or bathochromic shift in wavelength was noted, indicating that CHQF (chelating quenched fluorescence) via PET were the most likely mechanisms of fluorescent quenching. CHQF is the quenching of fluorescence upon metal binding or coordination and can occur via PET, ICT, ISC or isomerization .[43]

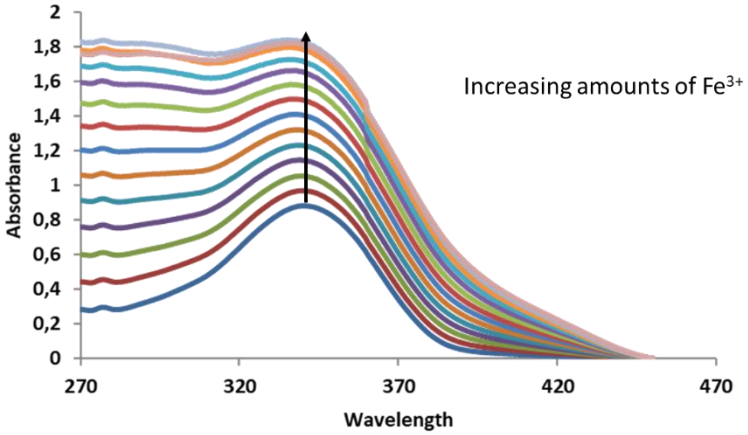

Figure 11. UV-Vis titration of **S1** with Fe^{3+} in acetonitrile.

Determination of fluorescence quenching process, association constant and detection limit.

To understand the quenching process of **S1** by Fe^{3+} in both water and acetonitrile, the observed decrease in fluorescence was followed using the linear Stern-Volmer equation. Initially, the equation for dynamic quenching was used to determine the value for K_{SV} as well as the limit of detection. Figure 12 shows the results for the plot of the titration of **S1** with Fe^{3+} in water following the linear equation: $F_0/F = 1 + K_{SV}[Q]$. Although the value for the regression line indicates correlation over the entire concentration range, the slight sigmoidal shape to the curve may indicate that different modes of quenching could be occurring. The detection limit in water and acetonitrile was calculated to be 3.6 & 5 µM whilst the value for the Stern-Volmer constant (K_{SV}) was 1.32 x 10^4 M^{-1} and 1.28 x 10^4 M^{-1} respectively.

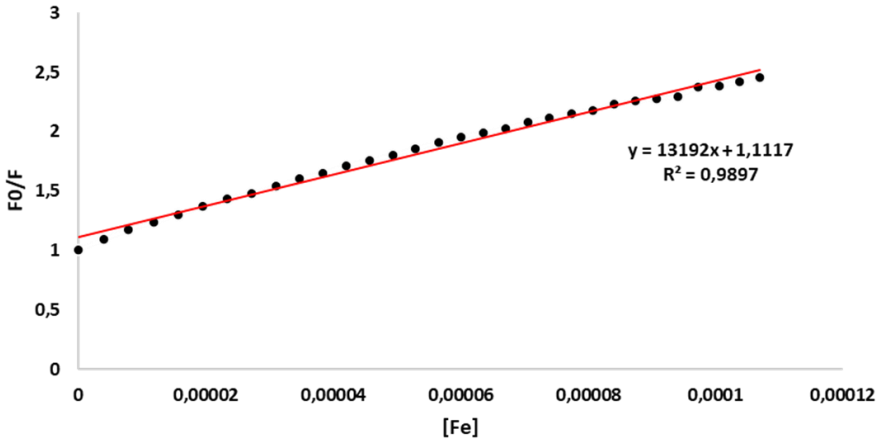

Figure 12. Plot of **S1** and Fe^{3+} in water following the linear Stern Volmer equation.

Benesi-Hildebrand calculations for S1 with Fe^{3+}

The Benesi-Hildebrand (BH) method for evaluation of the association constant and binding ratio was used for the titration of **S1** with increasing amounts of Fe^{3+} in water and acetonitrile. The plot of $1/I^0$-I vs $1/[Fe^{3+}]$ resulted in a positive linear graph with a good regression coefficient of R^2= 0.9962 and 0.9993 in water (Figure 13), and acetonitrile, respectively. The association coefficient, K_a, was calculated from the ratio of the

intercept to the slope of the graph. The values for the association constants and theoretical binding ratios for **S1** in water and acetonitrile are shown in Table 2. Based on the observed straight line of the plot, it could be concluded that the binding between the chemosensor and metal occurs in a 1:1 ratio.[44] This was later verified by Jobs Plot analysis.

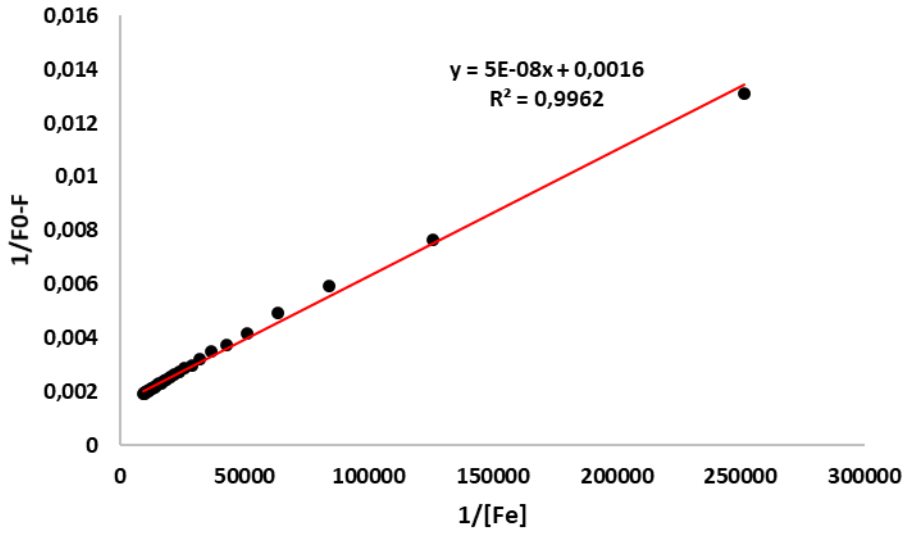

Figure 13. Benesi-Hildebrand plot of **S1** with Fe^{3+} in water.

Table 2. Association constants and binding stoichiometry of **S1** in water and acetonitrile

S1	Ka values (x10^4) M^{-1}	R^2 value	Suggested binding stoichiometry
Water	3.3	0.9962	1:1
Acetonitrile	4.9	0.9993	1:1

The association/binding coefficient gives an indication of the strength of the chemosensor-ligand bond. Evidently, **S1** displayed a larger association constant in acetonitrile than in water. This appreciable value for Ka in both water and acetonitrile may explain why **S1** was selective towards Fe^{3+} even within the presence of all other competing metal cations. This may further clarify why **S1**-Fe^{3+} binding was not reversible in the presence of EDTA. This will be discussed later with computational data.

Explanation of quenching process by Perrin sphere of action model.

The linear Stern-Volmer equation for dynamic/collisional quenching is applicable if the experimental results show linear variation over the entire concentration range. The slight deviance from linearity (sigmoidal shape) in Figure 12 suggests that the quenching mechanism is not purely collisional, and this may be attributed either to the ground state complex formation, a combined collisional and static quenching system or to the Perrin and modified sphere of action static quenching models.

For a combined collisional and static quenching model, a plot of $\left[\frac{F_o}{F} - 1\right]\frac{1}{[Q]}$ vs [Q] should yield a straight line, however, the experimental data did not fit the equation as shown by a poor regression coefficient. This

indicates that the quenching behaviour cannot be explained by the combined dynamic and static quenching mechanism alone.

The slight upward curvature of the plot at lower concentrations indicates that some static quenching may be taking place, or something that is called "the quenching sphere of action" (SOA), meaning that the analyte is capable of quenching the system within a specific radius of the receptor motif. The downward curvature at the higher quencher concentrations may result from the limited accessibility of the quencher to the fluorophore. For quenching within rigid solutions, Perrin introduced the concept of an “active sphere”, i.e., a volume of interaction around a quencher molecule such that a fluorophore excited within this volume is instantaneously quenched.[45] The values for K_p (Perrin constant), Perrin radius (Å) and detection limits (µM) were determined over the linear quencher-concentration range of 4 – 20 µM of 0.001 M Fe^{3+} solution. The calculated values are shown in Table 3.

Table 3. Values for constants and detection limits (µM) using the Perrin and Sphere of Action methods. The detection limit via the linear Stern-Volmer method is also included for comparison

S1	Kp ($x10^4$ M^{-1})	LOD (Linear Stern Volmer) µM	LOD (Perrin method µM)	Perrin Radius (Å)
Water	1.42	3.64	1.41	4.62
Acetonitrile	1.47	5.05	2.63	4.67

LOD = Limit of Detection

Evidently, the value for the detection limit via the Perrin sphere of action method is more than half of that determined by the linear Stern-Volmer method. This shows how care must be taken when determining the correct mode of quenching as it can have a drastic effect on the reported outcome. In addition, the size of **S1** from the methoxy derivative to the end of the phenyl functionality was determined by computational analysis. The length of the molecule was calculated to be 18. 037 Å. The diameter of the quenching sphere (9.2 Å) resides perfectly within this calculated distance.

Quantum yield studies

The fluorescence quantum yield (ϕ) of **S1** was evaluated using anthracene as a standard fluorophore with a known ϕ_S = 0.27 in ethanol. **S1**, in acetonitrile as the solvent, and the standard were excited using the same excitation wavelength (340 nm) and their absorbance were tuned to *ca.* 0.05 nm at the excitation wavelength. The integrated areas under the emission spectra were obtained using fl. Winlab software and the fluorescence quantum yields (ϕ) were calculated in accordance with equation (1)

$$\frac{\phi_X}{\phi_S} = \left[\frac{A_X}{A_S}\right]\left[\frac{Abs_S}{Abs_X}\right]\left[\frac{\eta_X}{\eta_S}\right]^2 \quad (1)$$

where ϕ_X and ϕ_S are the respective fluorescence quantum yield of the samples and standard, A_X and A_S are the integrated areas under the emission spectra of the samples and standard, Abs_X and Abs_S are the optical densities at the excitation wavelength of both samples and standards while ŋx and ŋs are the respective refractive indices of the solvents used for sample analysis and standard.

The quantum yield (ϕ) of **S1** was determined to be 0.71. This value indicates a bright fluorophore with high emissive intensity.

Reversibility studies of S1 for sensing Fe^{3+}

The reversibility of **S1** was investigated using the hexadentate chelating ligand ethylenediaminetetraacetic acid (EDTA). A partially quenched solution of **S1** with Fe^{3+} was titrated with a 0.01 M solution of EDTA. After the addition of up to 100 ul of the EDTA solution, there was still no drastic change in the emission spectra of the complex, suggesting a stronger interaction between **S1** and Fe^{3+} than that of Fe^{3+} and EDTA (Figure 14).

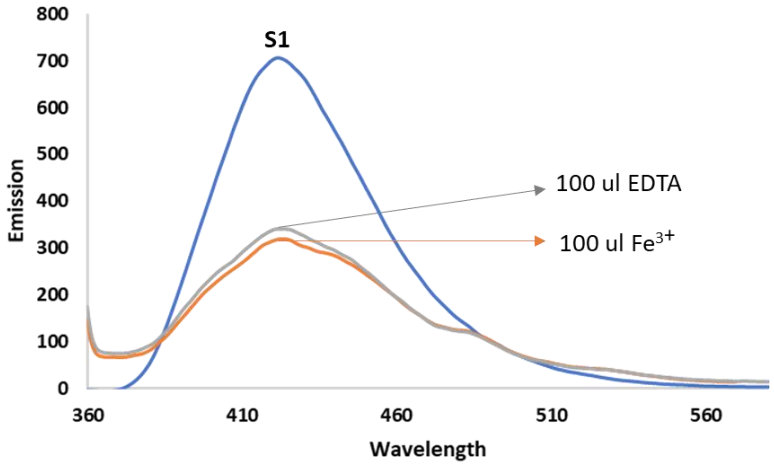

Figure 14. Titration of partially quenched **S1**-Fe^{3+} system with 100 µL aliquot of 0.01 M solution EDTA.

Determination of the binding stoichiometry using Job plots

Stock solutions of equal concentrations (0.01 M) of **S1** and Fe^{3+} were prepared. The molar fractions of **S1** and Fe^{3+} were varied whilst keeping the total concentration constant for each run. The emission spectra for increasing and decreasing amounts of Fe^{3+} were recorded in both acetonitrile and water. Job plots were constructed by plotting the maximum emission vs molar fraction of Fe^{3+} (Figure 15). The plots indicated that both the acetonitrile and water experiments gave a 1:1 chemosensor-metal binding ratio.

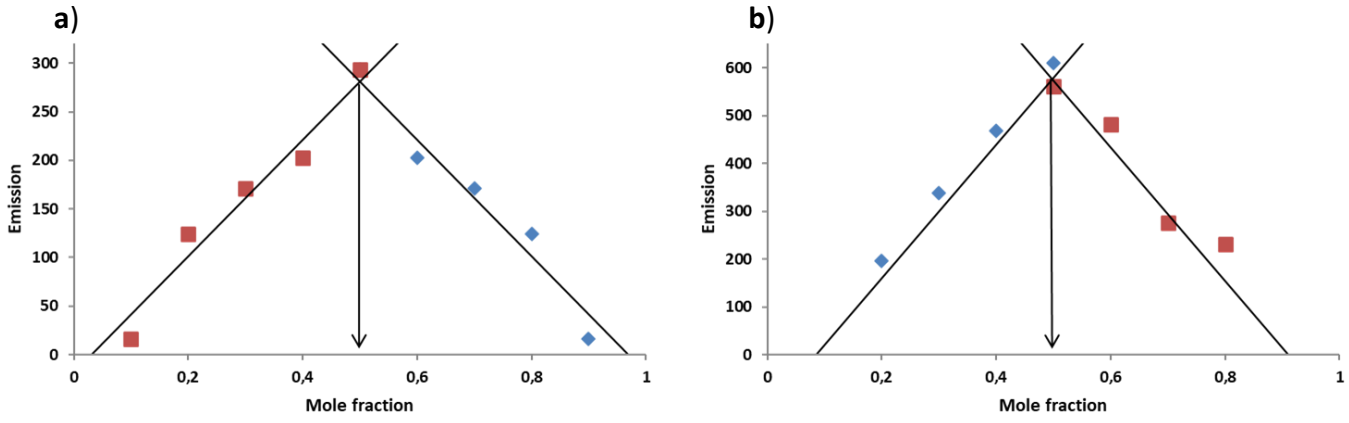

Figure 15. Jobs plot of **S1** and Fe^{3+} in a) water b) acetonitrile. Excitation conducted at 340 nm.

pH Studies

The sensing capabilities of **S1** towards Fe^{3+} were observed at the original pH of the solution. To analyze the effect of pH variations on sensing abilities, studies at different pH values were conducted. Different arrays of store-bought buffer solutions with pH of 10, 5, and 4 were utilized for the study. Addition of 6 µL of a 10 µM stock solution of **S1** to a non-buffered solution was compared to that of an equal aliquot of **S1** in a buffered solution. This was further compared with **S1** in each buffered solution with the addition of 20 µL aliquots of 0.01 M Fe^{3+} stock solution. These buffer solutions were chosen as they reflect the pH range of common wastewater from industrial processes and acidic mine drainage.[46–48] Results show that the chemosensing responses upon Fe^{3+} additions are constant in acidic and basic pH solutions. (Figure 16).

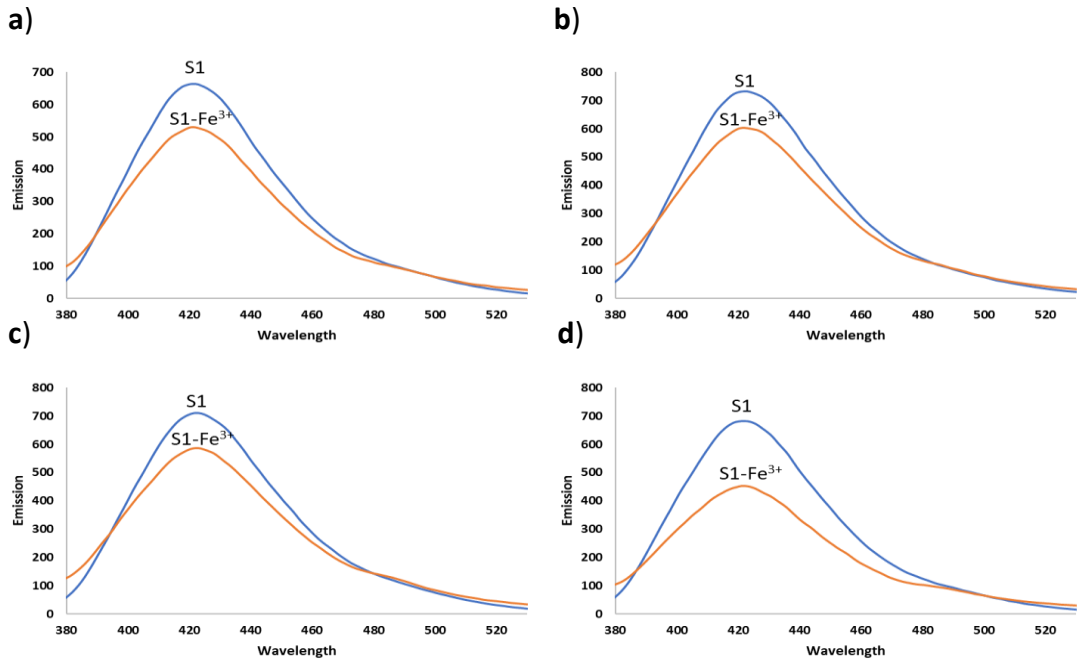

Figure 16. Effect of pH on **S1** and Fe^{3+} quenching behavior at (a) original pH, (b**)** pH 4, (c) pH 5, and (d) pH 10.

Proposed binding site between S1 and Fe^{3+}

It has been observed that the triazole ring can coordinate with metal ions *via* the N2 nitrogen atom to form stable complexes when there are neighboring assisting groups.[49–51] It was proposed that the interaction between the chemosensor and the metal ion occurs between the coumarin carbonyl and triazole nitrogen *via* a stable pseudo-six-membered ring as shown in Figure 17. The complexation affinity was attributed to the N-2 nitrogen lone electron pair donation from the triazole ring to the metal ion, assisted by a lone pair of electrons from the coumarin-carbonyl group.

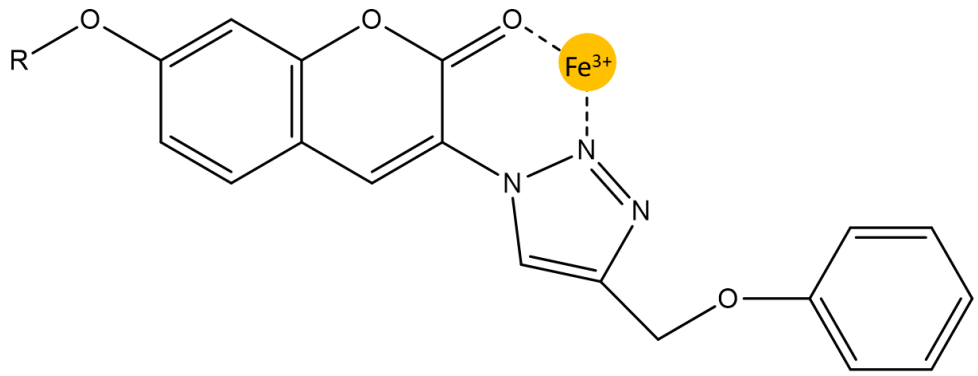

Figure 17. Proposed stable six-membered ring formation between **S1** with a Fe^{3+} ion.

The proposed binding site was investigated via ^{1}H NMR and ^{13}C NMR analysis. Initial titrations of **S1** with aliquots of $Fe(NO_3)_3$ displayed no shift in proton signals. Additionally, the peaks became less resolved as more Fe^{3+} was added (Figure 18). This indicated that the complexation of **S1** with Fe^{3+} does not affect the hydrogen atoms of **S1**.

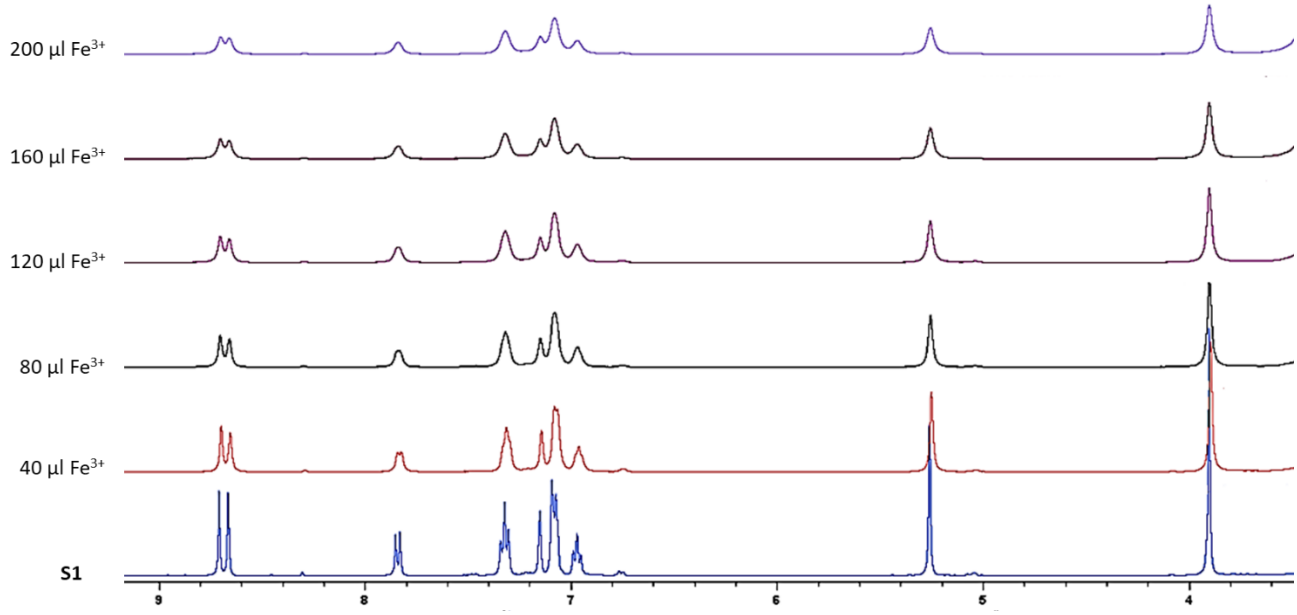

Figure 18. ^{1}H NMR titration of **S1** with $Fe(NO_3)_3$ in d_6-DMSO.

In addition to ^{1}H NMR analysis, ^{13} C NMR analysis was utilized to investigate the possible involvement of the triazole carbon double bond in metal complexation. It is well known that alkene and alkyne ligands can be involved in binding modes via σ- and π-electrons in organometallic complexes.[52] Furthermore, it has been reported that the C5 atom in the triazole ring can be involved in metal coordination.[53] The carbon spectrum of **S1** was compared to that of **S1** with 200 µl of Fe^{3+}. Notably, two peaks displayed pronounced shifts. These peaks were attributed to the two carbon atoms of the triazole ring. One of the carbon signals has shifted upfield whilst the other has shifted downfield. During this possible complexation, triazole-carbon labeled **A** has become more nucleophilic, resulting in an upfield shift, whilst carbon **B** is slightly electrophilic, leading to a shift downfield. This electron-density shift from **B** towards **A** may facilitate an interaction with the Fe^{3+} ion. In

addition, the coumarin carbon **C** displays no noticeable shift in the spectrum of the complex. It is, therefore, proposed that the lone pair of electrons from the oxygen atom could be taking part in the complexation rather than π-electrons from the carbon-oxygen double bond, forming a stable pseudo-6-membered ring between the C=O lone pair, Fe^{3+}, and triazole-carbon **A** (Figure 19).

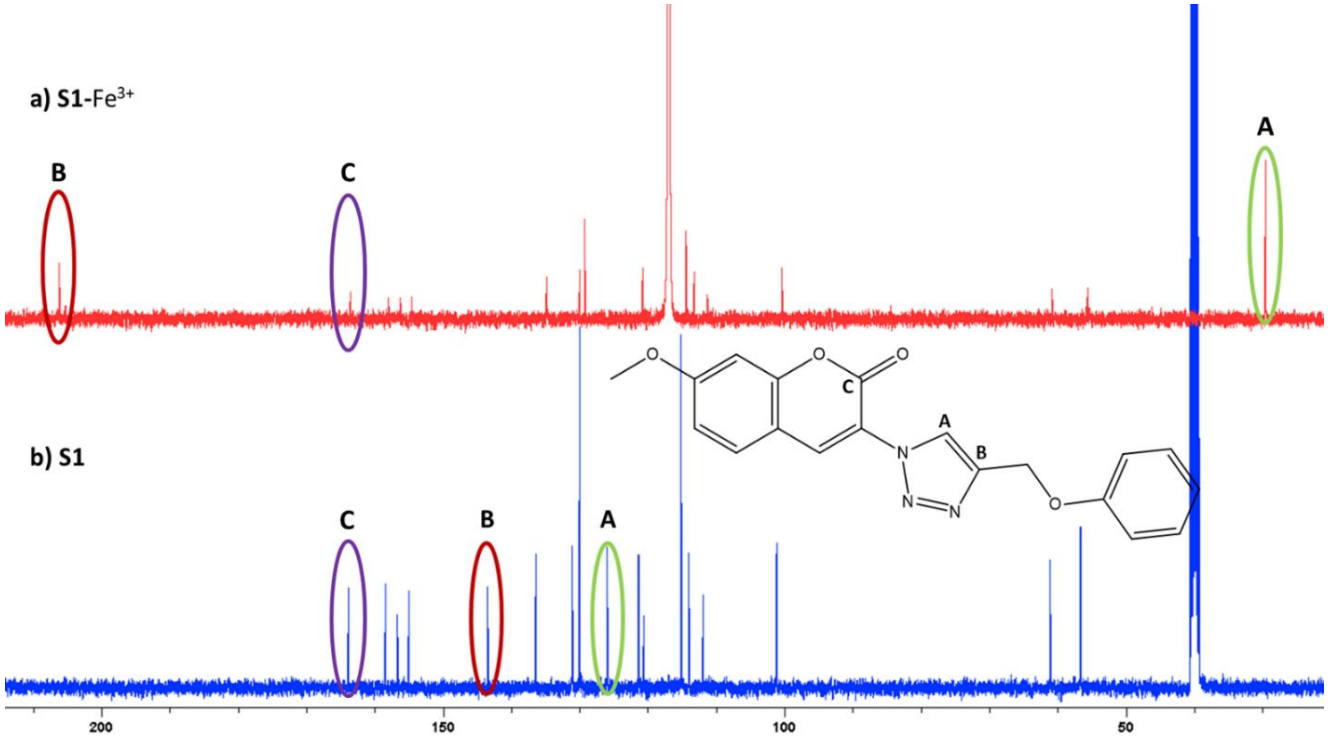

Figure 19. ^{13}C NMR spectra of a) **S1**-Fe^{3+} complex and b) **S1**. Inset structure: Conformation of the triazole functionality relative to the coumarin carbonyl to facilitate Fe^{3+} coordination.

From the reported triazole N-2 involvement in metal coordination from the literature, and the observed triazole carbon shift in Figure 19, two possible coordination conformations are now proposed (Figure 20). Computational analysis was therefore used to reconcile the most viable conformation for Fe^{3+} coordination with **S1**.

a)

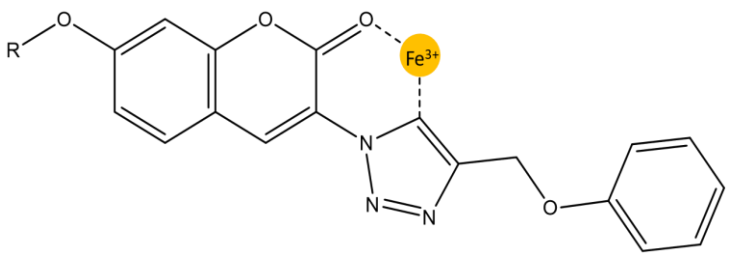

b)

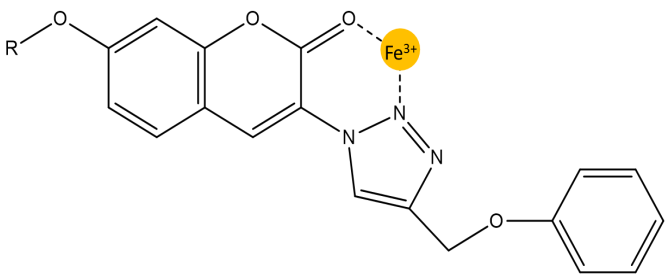

Figure 20. Two proposed coordination modes via a) triazole C-5 and coumarin-carbonyl and b) triazole N-2 atom and coumarin-carbonyl.

Computational analysis of S1

Computational analysis was utilized as a means of verification between experimental and theoretical outcomes. Calculations of most energetically preferred conformation (DFT B3LYP/6-31G), sensor-metal bond energies and ligand-metal bond energies (Molecular Mechanics MMFF) were conducted to verify the trends that were observed. Calculations were conducted using Spartan '10 V1.10.

Comparison of most stable conformation of S1 to XRD results

Molecular modeling studies were implemented to determine the lowest energy conformer of **S1** at the density-functional theory (DFT) level. This conformation was compared to that of the single crystal XRD data. Results from these computational calculations are in very close agreement with the observed crystal structure (Figure 21). The calculated energy of **S1** in this specific conformation was -3145754.12 kJ/mol, indicating the appreciable stability of **S1**. Although the calculated and observed conformations are not completely identical, the differences can be reconciled when the medium, and interactions between other molecules, are considered. These differences could arise as the calculations are carried out on one compound (in vacuum) whereas the crystal structure determination takes multiple factors into consideration, such as multiple compounds close to each other (proximity), solvents present (medium), forces and the interactions between them, and their packing arrangement.

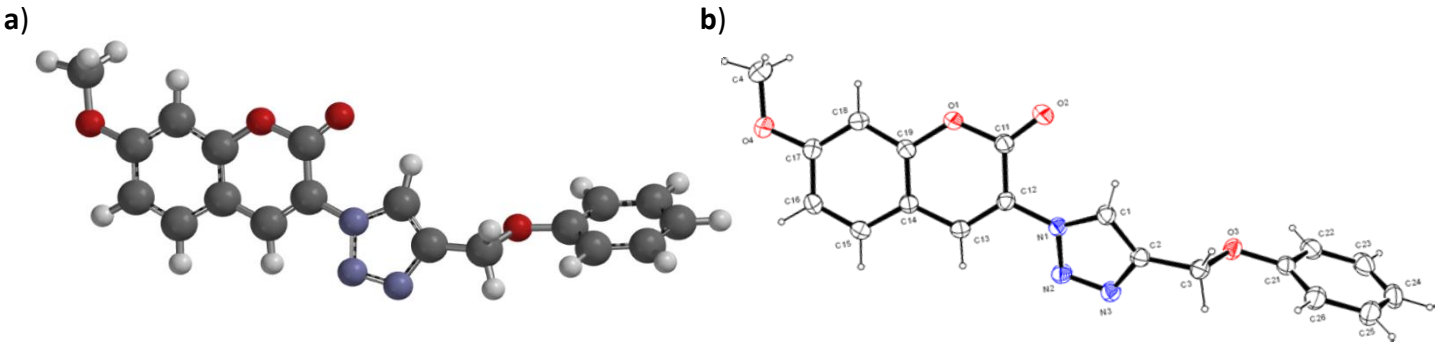

Figure 21. a) Computationally calculated most stable conformation, and b) experimental XRD results of **S1**.

Reconciliation of binding site of S1 with Fe^{3+}

Once the most stable conformer of **S1** was established, it was used for binding studies towards Fe^{3+}. Calculations conducted at Molecular Mechanics level (MMFF) displayed the proposed twisting of the triazole nitrogens towards the coumarin carbonyl to facilitate the pseudo 6-membered ring between the triazole N-2 triazole nitrogen and the lone pair of the coumarin carbonyl oxygen (Figure 22). This agrees with what has previously been reported in literature regarding the binding properties of the triazole nitrogen atoms towards metal complexation in the presence of nearby assisting groups. Notably the phenyl ring has twisted towards the Fe^{3+} cation, however, hydrogen bond calculations showed that no hydrogen bonding was taking place. This is also verified by the ^{1}H NMR titration analysis.

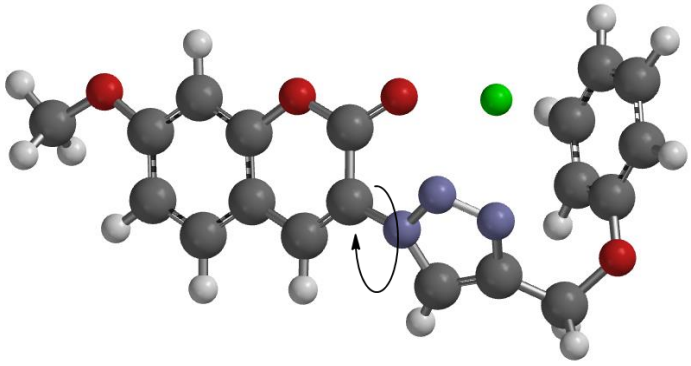

Figure 22. Computational conformation of **S1**-Fe^{3+} binding scenario.

In addition to computational analysis, titration data of **S1** with a more concentrated 0.01 M Fe^{3+} solution was able to verify the number of binding sites present between the chemosensor and metal cation. According to equation (2), a plot of Log[F_0-F/F] vs Log[Q] should yield a straight line with the gradient equal to n, where n is the number of binding sites present.[54] A straight line occurs when the predominant mode of quenching occurs via a static process. The regression coefficient indicated good linearity and the number of binding sites was shown to be equal to 1 (Figure 23). This agrees with what has been shown computationally and what has been postulated whereby the N2 triazole nitrogen is the main contributor of binding electrons towards Fe^{3+} and is assisted by the lone electron pair of the coumarin carbonyl.

$$Log\left[\frac{F_0 - F}{F}\right] = LogK + nLog[Q] \quad (2)$$

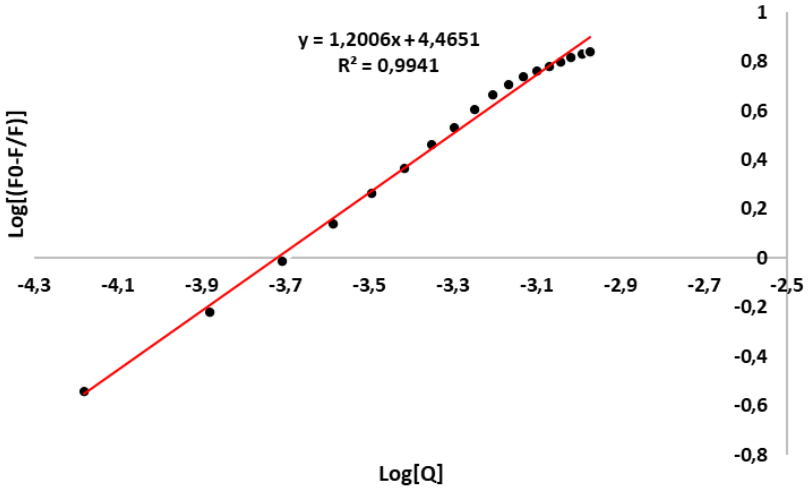

Figure 23. Logarithmic plot of the fluorescence quenching of **S1** with various amounts of Fe^{3+} in excitation wavelength of 340 nm.

Although the computed binding between **S1** and Fe^{3+} is promising, it does not explain the shifting observed in the triazole carbon atoms as seen in the ^{13}C NMR analysis. As stated previously, the carbon double bond of the triazole ring can take part in binding due to its electron density. The nitrate counterion from $Fe(NO_3)_3$ was computed with the most stable conformer of **S1** in water as the medium. The computation of the sensor and anion displayed the same twisting of the triazole ring nitrogen atoms towards the coumarin carbonyl (as seen in the **S1**-Fe^{3+} computation), and the placement of the nitrate anion near the site of the triazole carbon double bond (Figure 24). Hydrogen bond calculations indicated no hydrogen bonding between the nitrate and **S1**. It is hypothesized that the water molecules, together with the carbon double bond of the triazole, form a stable complex with the nitrate counterion resulting in the observable shift in the ^{13}C NMR spectrum. The strong interaction of **S1** with Fe^{3+} could make the carbon double bond π-electrons more readily available for bonding due to the shift in electron density in the triazole ring towards Fe^{3+}.

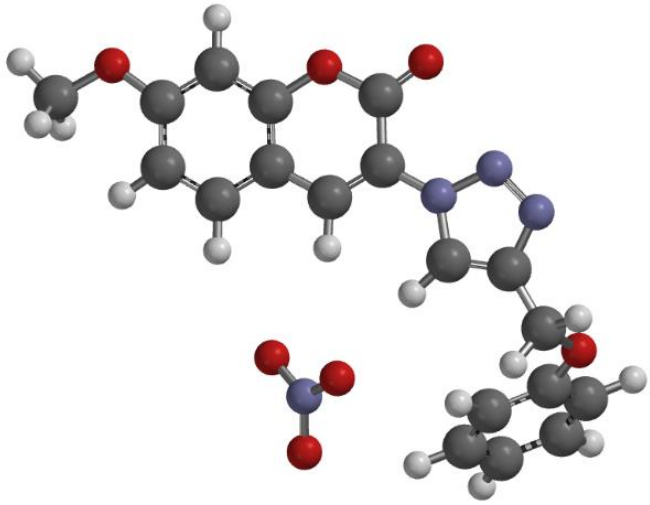

Figure 24. Computed conformation of **S1** in the presence of nitrate counterions. Computation conducted in water as a medium.

Verification of selectivity trends of S1 with Fe^{3+}

The most energetically stable conformer of **S1** was used to reconcile the selectivity trend seen in the experimental data. As stated, **S1** was selective to Fe^{3+} despite the presence of other competing metal ions. The proposed site of metal binding in the cavity between the triazole nitrogen and coumarin-carbonyl was used for these calculations. Water was used as the medium in which the energies were calculated. The energy of the **S1**-Fe^{3+} complex at this proposed position (at Molecular Mechanics level) was found to be -846.22 kJ/mol, an acceptably low, and, therefore, energetically-stable-binding scenario. In addition, the calculated energies of **S1**-Hg^{2+} and **S1**-Cu^{2+} were considerably higher than that of **S1**-Fe^{3+}, thereby, reconciling the selectivity seen between **S1** and Fe^{3+} in the presence of competing metal cations. The complex energies between **S1** and the three tested metal cations are shown in Table 5.

Table 5. Calculated complex energies between **S1** and three competing metal cations

Metal Cation	Fe^{3+}	Cu^{2+}	Hg^{2+}
Calculated complex energy (kJ/mol)	-846.22	-372.47	48.55

Computation of reversibility studies of S1 - Fe^{3+} with EDTA

Computational analysis was further employed to reconcile the trends observed in the reversibility studies between **S1**-Fe^{3+} and the hexadentate ligand, EDTA. Titration of EDTA with **S1**-Fe^{3+} showed that Fe^{3+} was not released following continuous EDTA additions. Calculation of complex energies between EDTA-Fe^{3+} and **S1**-Fe^{3+} were performed. Table 6 shows the energies of the ligands and ligand-metal complexes calculated using molecular mechanics (MMFF).

Table 6: Energies of the ligand-Fe^{3+} complexes

Ligand / Ligand-Metal complex	Complex energy (kJ/mol)
EDTA	467.81
EDTA-Fe^{3+}	-350.85
S1-Fe^{3+}	-846.22

The complex energy between **S1** and Fe^{3+} is more than two times lower than that of EDTA and Fe^{3+}. This lower energy complex prevents the abstraction of the Fe^{3+} ion from the binding sites on **S1**. For this reason, it is evident why Fe^{3+} was not reversible in the presence of increasing amounts of EDTA.

Conclusions

Coumarin derivatives with triazole moieties, which can function as fluorescent chemosensors, were synthesized utilizing "click chemistry" protocol. One derivative displayed exceptional selectivity towards Fe^{3+} in the presence of other competing metal cations and an appreciably low detection limit of 1.4 μM Fe^{3+}. The triazole N-2 nitrogen atom, together with the coumarin carbonyl lone electron pair, provide coordination sites for the Fe^{3+} ion. Complexation is believed to occur in a stable pseudo-6-membered-ring-like conformation. The coumarin moiety plays a dual role as a signaling unit and cation binding site.

Experimental Section

Measurements

All starting materials and solvents were purchased from Sigma Aldrich or Merck and used as received without further purification unless stated. ^{1}H NMR and ^{13}C NMR spectra were recorded on a Bruker Advance DPX 400 (400 MHz). NMR samples were prepared in deuterated solvents ($CDCl_3$, CD_3CN and DMSO-d_6). The samples were run at room temperature. Coupling constants (*J*) are given in Hz, whilst chemical shifts are expressed in parts per million (ppm) using TMS as internal reference. FT-IR spectra were taken on a Bruker TENSOR 27 FT-IR spectrometer. Column chromatography was performed using silica gel (particle size 0.040-0.063 mm) while

thin layer chromatography (TLC) analyses were performed on pre-coated silica gel 60 F254 aluminum sheets (0.063 - 0.2 mm/70 - 230 mesh); compounds were detected by observation under UV light and/or exposure to iodine vapour. The emission spectra were recorded at room temperature in acetonitrile (CH_3CN) using a Perkin Elmer LS 45 fluorescence spectrometer and a 1-cm quartz cell. Stock solutions of the chemosensors were prepared by dissolving the samples in acetonitrile and diluting them to the desired concentrations.

Materials

Stock solutions of triazolyl-coumarin derivatives **S1** and **S2** were prepared by dissolving the respective samples in 25 mL of acetonitrile to afford stock solutions of 0.001 M. Deionized water was used to prepare solutions of metal ions to the concentration of 0.01 M which were then diluted further for titration studies. All metal ion solutions were prepared using nitrate salts. The titration experiments were performed in a 3-mL quartz cuvette using diluted solutions of compounds **S1** and **S2**. Spectroscopic measurements were performed after each addition of an aliquot of selected metal ion solution.

Synthesis of 3-azidocoumarin derivative (1). 3-Azidocoumarin derivatives (**1**) were synthesized according to literature procedures.[55]

Synthesis of 1-(prop-2-ynyloxy)benzene (2). A solution of phenol (5.0 g, 53 mmol) and K_2CO_3 (14.7 g, 106 mmol) in dry acetone (50 mL) was refluxed under nitrogen atmosphere for 4 hours to afford sodium alkoxide ions. The reaction mixture was cooled to room temperature and propargyl bromide (6.32 g, 53 mmol) was added dropwise. The resulting mixture was left to stir at room temperature for 24 hours. The THF was removed under reduced pressure and the residue dissolved in water and extracted with ethyl acetate (3 x 40ml). The extracts were combined, dried over anhydrous Na_2SO_4, and the solvent was removed under reduced pressure. The crude product was purified by column chromatography using hexane: ethyl acetate (80:20) as eluent to afford the pure product as a light-yellow oil (4.23 g, 60%). ^{1}H NMR: ($CDCl_3$, 400MHz) δ_H: 2.56 (s, 1H), 4.73 (s, 2H), 7.05 (m, 3H), 7.36 (t, 2H, *J* 7.6), ^{13}C NMR ($CDCl_3$, 100.6 MHz) δ_C: (75.52, C-1), (78.71, C-2), (55.77, C-3), (157.60, C-4), (114.96, C-5), (129.52, C-6), (121.62, C-7), IR ν_{max} (cm^{-1}): 3290 (alkyne C-H), 2116 (alkyne C≡C), 1212 (C-O-C).

Synthesis of triazolyl coumarin chemosensors S1 and S2. A mixture of coumarin-azide derivatives (**1**) (0.3 g, 148 mmol (OH); 0.3 g, 138 mmol (OCH_3)), 1-(prop-2-ynyloxy)benzene (**2**) (0.3 g, 227 mmol), $CuSO_4.5H_2O$ (0.01 g, 0.05 mmol), sodium ascorbate (0.02 g, 0.10 mmol) and N,N,N′,N′′,N′′-pentamethyldiethylenetriamine (PMDETA) (0.02 g, 0.10 mmol) in THF (100 mL) was stirred at room temperature for 48 hrs. The solvent was evaporated under vacuum and the residue dissolved in ethyl acetate (30 mL), washed with water (3x30ml) and dried over anhydrous Na_2SO_4. The organic layer was evaporated under vacuum and crude product purified by recrystallization from DCM (5 mL) and petroleum ether (40 mL) to give the desired triazolyl coumarin derivatives **S1** (0.297 g, 62%) and **S2** (0.119 g, 24%). Compound **S1:** ^{1}H NMR: (CD_3Cl_3, 400MHz) δ_H: 3.94 (s,3H); 5.26 (s, 2H); 7.04 (m, 5H); 7.35 (t, 2H, *J* 7.3); 7.72 (d, 1H, *J* 8.5); 8.49 (s, 1H); 8.55 (s,1H). ^{13}C NMR (DMSO-d_6, 100.6 MHz) δ_C: 56.67; 61.11; 101.19; 111.94; 114.02; 115.17; 120.65; 121.39; 125.97; 130.00; 131.10; 136.46; 143.47; 155.03; 156.69; 158.45; 163.91. Compound **S2**: ^{1}H NMR: (DMSO-d_6, 400MHz) δ_H: 5.25 (s, 2H); 6.94 (m, 5H); 7.08 (d, 2H, *J* 7.8); 7.32 (t, 2H, *J* 7.32); 7.75 (d, 1H, *J* 8.2); 8.61 (s, 1H); 8.68 (s, 1H); 10.91 (s, 1H). ^{13}C NMR (DMSO-d_6, 100.6 MHz) δ_C: 61.12; 102.64; 110.79; 114.77; 115.16; 119.75; 121.38; 125.99; 130.00; 131.45; 136.98; 143.41; 155.15; 156.80; 158.45; 162.96.

Acknowledgements

For this work we acknowledge the Council for Scientific and Industrial Research (CSIR) and Nelson Mandela University (NMU) for funding and facilities to carry out this project.

Supplementary Material

Supplementary material containing copies of FT-IR, ^{1}H NMR and ^{13}C NMR spectra, and time-delay UV-Vis fluorescence studies plots of 3-azidocoumarin derivatives (1), and Benesi-Hildebrand plot of (1) in acetonitrile can be found in the online version.

References

1. Madhu, P.; Sivakumar, P. *J. Mol. Struct*. **2019**, 1193, 378–385. https://doi.org/10.1016/j.molstruc.2019.05.044
2. Pipattanawarothai, A.; Trakulsujaritchok, T. *Dyes Pigment*s **2020**, 173, 1–9. https://doi.org/10.1016/j.dyepig.2019.107946
3. Wang, Y.; Wu, H.; Wu, W.N.; Mao, X.J.; Zhao, X.L.; Xu, Z.Q.; Xu, Z.H. *Spectrochim. Acta. A-M*. **2019**, 212, 1–9. https://doi.org/10.1016/j.saa.2018.12.017
4. Ghorai, P.; Pal, K.; Karmakar, P.; Saha, A. *Dalton Trans*. **2020**, 49, 4758–4773. https://doi.org/10.1039/C9DT04902A
5. Sarih, N.M.; Ciupa, A.; Moss, S.; Myers, P.; Slater, A.G.; Abdullah, Z.; Tajuddin, H.A.; Maher, S. *Sci. Rep*. **2020**, 10, 1-12. https://doi.org/10.1038/s41598-020-63262-7
6. Yenilmez Ciftci, G.; Yilmaz, S.; Bayik, N.; Şenkuytu, E.; Nur Kaya, E.; Durmus, M.; Bulut, M. *Turk. J. Chem*. **2020**, 44, 64–73. https://doi.org/10.3906/kim-1908-51
7. Zhang, R.; Xu, Z.; Hu, L.; Song, Y. J. *Mol. Struct.* **2020**, 1204, 1–8.
8. Chereddy, J.J.; Ren, S.S.; Chen, Y.; Su, X.; Zhong, D.; Mori, Z.; Inoue, T.; Wu, Y.; Yang, W. *J. Photochem. Photobiol. A Chem*. **2018**, 355, 78–83. https://doi.org/10.1016/j.jphotochem.2017.10.043
9. Li, Y.; Pan, W.; Zheng, C.; Pu, S. *J. Photochem. Photobiol. A Chem*. **2020,** 389, 1–8.
10. Tang, X.; Wang, Y.; Han, J.; Ni, L.; Wang, L.; Li, L.H.; Zhang, H.Q.; Li, C.; Li, J.; Li, H. *Spectrochim. Acta.* **2018**, 191, 172–179. https://doi.org/10.1016/j.saa.2017.10.018
11. Dwivedi, S.K.; Gupta, R.C.; Ali, R.; Razi, S.S.; Hira, S.K.; Manna, P.P.; Smart, A.M. *J. Photochem. Photobiol. A Chem*. **2018**, 358, 157–166. https://doi.org/10.1016/j.jphotochem.2018.03.011
12. Sousa, L.; Oliveira, M.M.; Pessôa, M.T.C.; Barbosa, L.A. *Clin. Chim. Acta*. **2020**, 504, 180–189. https://doi.org/10.1016/j.cca.2019.11.029

13. Said, A.I.; Georgiev, N.I.; Bojinov, V.B. *Spectrochim. Acta A*. **2018**, 196, 76–82. https://doi.org/10.1016/j.saa.2018.02.005
14. Zhang, M.; Gong, L.; Sun, C.; Li, W.; Chang, Z.; Qi, D. *Spectrochim. Acta Part A Mol. Biomol. Spectrosc*. **2019**, 214, 7–13. https://doi.org/10.1016/j.saa.2019.01.089
15. Balachandra, A.L.; Deepthi, A.; Sunees, C.V. *Luminescence*. **2020**, 35, 62–68. https://doi.org/10.1002/bio.3695
16. Joseph, R.; Asok, A.; Joseph, K. *Spectrochim. Acta Part A Mol. Biomol. Spectrosc*. **2020**, 224, 1–6. https://doi.org/10.1016/j.saa.2019.117390
17. Chen, Z.E.; Zang, X.F.; Yang, M.; Zhang, H. *Spectrochim. Acta Part A Mol. Biomol. Spectrosc*. **2020**, 234, 1-7.
18. Hang, M.; Shen, C.; Jia, T.; Qui, J.; Zhu, H.; Gao, Y. *Spectrochim. Acta Part A Mol. Biomol. Spectrosc*. **2020**, 231, 1-7.
19. Atkins, L.A.; McNaughton, S.A.; Spence, A.C.; Szymlek-Gay, E.A. *Eur. J. Nutr*. **2020**, 59, 175–184. https://doi.org/10.1007/s00394-019-01897-7
20. Shubham, K.; Anukiruthika, T.; Dutta, S.; Kashyap, A.V.; Moses, J.A.; Anandharamakrishnan, C. *Trends Food Sci. Technol*. **2020**, 99, 58–75. https://doi.org/10.1016/j.tifs.2020.02.021
21. Gao, G.Y.; Qu, W.J.; Shi, B.B.; Lin, Q.; Yao, H.; Zhang, Y.M.; Chang, J.; Cai, Y.; Wei, T.B. *Sens. Actuators B Chem*. **2015**, 213, 501–507. https://doi.org/10.1016/j.snb.2015.02.077
22. Wang, J.; Wei, T.; Ma, F.; Li, T.; Niu, Q. *J. Photochem. Photobiol. A Chem*. **2019**, 383, 1-9.
23. Şenkuytu, E. *Inorganica Chim. Acta.* **2018**, 479, 58–65. https://doi.org/10.1016/j.ica.2018.04.028
24. Pal, D.; Gede, M.; Moczar, I.; Baranyai, P. *Period. Polytech. Chem. Eng*. **2020,** 64, 20–36. https://doi.org/10.3311/PPch.14467
25. Deems, J.C.; Reibenspies, J.H.; Lee, H.S.; Hancoc, R.D. *Inorg. Chim. Acta.* **2020**, 499, 1-10. https://doi.org/10.1016/j.ica.2019.119181
26. Sun, X.Y.; Liu, T.; Sun, J.; Wang, X.J. *RSC Adv*. **2020,** 10, 10826–10847. https://doi.org/10.1039/C9RA10290F
27. Cao, D.; Liu, C.; Verwilst, P.; Koo, S.; Jangjili, P.; Kim, J.S.; Lin, W. *Chem. Rev*. **2019**, 119, 10403–10519. https://doi.org/10.1021/acs.chemrev.9b00145
28. Gao, Z.G.; Kan, C.; Liu, H.B.; Zhu, J.; Bao. X. *Tetrahedron*. **2019**, 75, 1223–1230. https://doi.org/10.1016/j.tet.2019.01.029
29. Singh, G.; Satija, P.; Singh, A.; Diksha, A.; Pawan, A.; Suman, A.; Sushma, A. ; Mohit, A. ; Soni, S. *Mater. Chem. Phys*. **2020**, 249, 1-10. https://doi.org/10.1016/j.matchemphys.2020.123005
30. Ngororabanga, J.M.V.; Du Plessis, J.; Mama, N. *Sensors* **2017**, 17, 1-13.
31. Sivakumar, K.; Xie, F.; Cash, B.M.; Long, Su.; Barnhill, H.N.; Wang, Q. *Org. Lett*. **2004**, 6, 4603–4606. https://doi.org/10.1021/ol047955x
32. Zhang, J.; Pang, Z.; Dong, C. *Indian J. Chem.* **2020**, 59, 895–903.
33. Bhagwat, A.A.; Sekar, N. *J. Fluoresc*. **2019**, 29, 121–135. https://doi.org/10.1007/s10895-018-2316-2
34. Bhalekar, S.B.; Bhagwat, A.A.; Sekar, N. *J. Fluoresc.* **2020**, 30, 565–579.

https://doi.org/10.1007/s10895-020-02506-1
35. Yadav, S.B.; Kothavale, S.; Sekar, N. *J. Photochem. Photobiol. A Chem*. **2019**, 382, 1-19.
36. Sato, K.; Sato, R.; Iso, Y; Isobe, T. *Chem. Commun*. **2020**, 56, 2174–2177. https://doi.org/10.1039/C9CC09333H
37. Yadav, S.B.; Sonvane, S.S.; Sekar, N. *Spectrochim. Acta - Part A Mol. Biomol. Spectrosc*. **2020**, 224, 1-17.
38. Ray, A.; Bhattacharya, S. *J. Mol. Liq.* **2020**, 299, 1-8. https://doi.org/10.1016/j.molliq.2019.112168
39. Ramamurthy, K.; Ponnusamy, K.; Chellappan, S. *RSC Adv.* **2019**, 10, 998–1006. https://doi.org/10.1039/C9RA10154C
40. Basu, N.; Mandal, D. *Photochem. Photobiol. Sci.* **2019**, 18, 1782–1792. https://doi.org/10.1039/C8PP00540K
41. Ray, A.; Sengupta, S.; Chattopadhyay, N. *J. Photochem. Photobiol. A Chem.* **2019**, 371, 433–443. https://doi.org/10.1016/j.jphotochem.2018.11.026
42. dos Santos, C.M.G.; McCabe, T.; Gunnlaugsson, *Tetrahedron Lett.* **2007**, 48, 3135–3139. https://doi.org/10.1016/j.tetlet.2007.03.061
43. Zhang, Z.; Wang, C.; Zhang, Z.; Luo, Y.; Sun, S.; Zhang, G. *Spectrochim. Acta - Part A Mol. Biomol. Spectrosc.* **2019**, 209, 40–48. https://doi.org/10.1016/j.saa.2018.10.022
44. Goswami, S.; Aich, K.; Das, A.K.; Manna, A.; Das, S. *RSC Adv*. **2013**, *3*, 2412–2416. https://doi.org/10.1039/c2ra22624c
45. Perrin, F.C.R. *Acad. Sci. Paris.* **1924**, 178, 1978.
46. Chen, H.; Xiao, T.; Ning, Z.; Li, Q.; Xiao, E.; Liu, Y.; Xiao, Q.; Lan, X.; Ma, L.; Lu, F. *Bioresour. Technol.* **2020**, 317, 1-11. https://doi.org/10.1016/j.biortech.2020.123985
47. Vélez-Pérez, L.S.; Ramirez-Nava, J.; Hernandez-Florez, G.; Talavera-Mendoza, O.; Escamilla-Alvarado, C.; Poggi-Veraldo, H.M.; Solorza-Feria, O.; Lopez-Diaz, J.A. *Int. J. Hydrog*. **2020**, 45, 13757–13766. https://doi.org/10.1016/j.ijhydene.2019.12.037
48. Sun, R.; Zhang, L.; Wang, X.; Ou, C.; Lin, N.; Xu, S.; Qiu, Y.Y.; Jiang, F. *Water Res*. **2020**, 185, 1-42. https://doi.org/10.1016/j.watres.2020.116230
49. Sumrra, S.H.; Sahrish, I.; Raza, M.A.; Ahmad, Z.; Zafar, M.N.; Cohan, Z.H.; Khalid, M.; Amed, S. Monatsh. Chem. **2020**, 151, 549–557. https://doi.org/10.1007/s00706-020-02571-z
50. Schlagintweit, J.F.; Dyckhoff, F.; Nguyen. L.; Jakob, C.H.G.; Reich, R.M.; Khun. F.E. *J. Catal*. **2020**, 383, 144–152. https://doi.org/10.1016/j.jcat.2020.01.011
51. Snyder, E.M.; Chowdhury, M.S.I.; Morrow, J.R. *Inorganica Chim. Acta.* **2020**, 509, 1-8.
52. Mulks, F.F.; Hashmi, A.S.K.; Faraji, S. *Organometallics.* **2020**, 39, 1814–1823. https://doi.org/10.1021/acs.organomet.0c00102
53. Radhakrishna, L.; Kunchur, H.S.; Namdeo, P.K.; Butcher, R.J.; Balakrishna, M.S. *Dalt. Trans.* **2020**, 49, 3434–3449. https://doi.org/10.1039/C9DT04302K
54. Ngororabanga, J.M.V.; Tshentu, Z R.; Mama, N. *J. Fluoresc.* **2020**, 1-13.

55. Sivakumar, K.; Xie, F.; Cash, B.M.; Long, Su.; Barnhill, H.N.; Wang, Q. *Org. Lett*. **2004**, 6, 4603–4606. https://doi.org/10.1021/ol047955x